Depth-resolved chemical speciation of a W-B_4C multilayer structure

Gangadhar Das,[1,2] A. G. Karydas,[3,4] Haranath Ghosh,[2,5] M. Czyzycki,[3,6] A. Migliori,[3] A. K. Sinha,[1,2] and M. K. Tiwari[1,2,*]

[1]*Synchrotrons Utilization Section, Raja Ramanna Centre for Advanced Technology, Indore 452013, Madhya Pradesh, India*

[2]*Homi Bhabha National Institute, Anushaktinagar, Mumbai 400094, India*

[3]*Nuclear Science and Instrumentation Laboratory, International Atomic Energy Agency, Vienna, Austria*

[4]*National Centre for Scientific Research "Demokritos", Institute of Nuclear and Particle Physics, Athens, P.O. Box 60037, 153 10 Agia Paraskevi, Greece*

[5]*Human Resources Development Section, Raja Ramanna Centre for Advanced Technology, Indore-452013, Madhya Pradesh, India*

[6]*AGH University of Science and Technology, Faculty of Physics and Applied Computer Science, Mickiewicza 30, 30-059 Krakow, Poland*

(Received 15 May 2017; revised manuscript received 30 September 2017; published 24 October 2017)

We report results of simultaneous x-ray reflectivity and grazing incidence x-ray fluorescence measurements in combination with x-ray standing-wave-assisted depth-resolved near-edge x-ray absorption measurements to reveal new insights on chemical speciation of W in a W-B_4C multilayer structure. Interestingly, our results show the existence of various unusual electronic states for the W atoms especially those near to the surface and interface boundary of a thin film medium as compared to those of the bulk. These observations are found to be consistent with the results obtained using first-principles calculations. Unlike the conventional x-ray absorption measurements the present approach has an advantage that it permits the determination of the depth-resolved chemical nature of an element in the thin-layered materials at atomic length scale resolution.

DOI: 10.1103/PhysRevB.96.155444

I. INTRODUCTION

Electronic states at the surface and interface boundary of a thin film medium significantly differ from those of the bulk due to strong orbital reconstruction or hybridization of near surface atoms [1]. Such a hybridization extensively modulates the physical properties of a thin film medium. Despite the recent advances in thin film growth methodology the interface boundary between two materials in a thin film cannot be realized distinctly due to atomic migration [2]. Surface and interface alteration due to atomic scale modulation of the orbital occupation is an active area of research to unravel insights on many correlated and uncorrelated physical phenomena, such as electronic and magneto transport properties and interlayer exchange coupling properties of various thin-layered materials in condensed matter physics research [3–9]. In order to achieve a detailed understanding about the electronic mechanism responsible for the observed physical properties in thin-layered materials it is often necessary to investigate and compare unusual behavior of orbital electrons in surfaces, interfaces, and bulk [1,3,10–12]. Probing surfaces and interfaces in a superlattice structure [13,14] can lead to a new opportunity to reveal unusual physical properties associated with a thin-layered material. Despite immense interest in this direction, no appropriate technique is available that can provide depth-resolved localized chemical information about a thin-layered material. The conventional absorption techniques suffer from the inherent technical limitations as they do not provide depth-resolved information about physical and chemical properties of nanostructured materials and their localization with respect to the substrate surface. Surface interface studies have had many surprises in the past and are still not fully understood [15–17]. For example, a recent work discovered the unknown origin of interfacial magnetism and superconductivity in nature communications [18]. Similarly electronic properties such as the density of states and the change of valance states at surface interface boundaries of thin film medium can be significantly different from bulk. The recent advances in the field of surface-interface analysis of thin-layered materials have spurred new experimental efforts to develop methods that are far more accurate as compared to conventional absorption methods.

The fluorescence-assisted x-ray standing-wave (XSW) technique has become the workhorse for the surface-interface aspects of condensed matter research. As a nondestructive probe, the XSW-induced fluorescence measurements at grazing incidence angles offer atomic scale depth resolution inside a thin film medium [19–26]. Recent advancements in various combined x-ray spectroscopy approaches have made it possible to obtain depth-resolved chemical information on surfaces and interfaces in a nondestructive manner. In our previous work we have shown that x-ray reflectivity (XRR) together with grazing incidence x-ray fluorescence (GIXRF) measurements can be used as a sensitive probe to evaluate depth-resolved microstructural parameters of a buried layer inside a W-B_4C multilayer structure [13]. It has been demonstrated that a slight diffusion of W into a B_4C layer significantly increases the density of the B_4C medium. Tungsten has an outer-shell electronic configuration of $5d^4\ 6s^2\ 6p^0$. Its $5d$ band remains partially filled in the case of divalent, trivalent, tetravalent, and pentavalent compounds and completely empty in the case of hexavalent compounds. Since the $5d$, $6s$, and $6p$ electronic levels are very close to each other, hybridization of these orbitals is energetically favorable in many tungsten compounds. Such hybridization significantly modulates the nature of these higher shell energy levels [27–31]. Hence, depth-resolved chemical speciation is often desirable to understand the underlying degradation pathways (*if any*) and their influence on the interfacial chemical changes in the case of a multilayer structure.

*mktiwari@rrcat.gov.in

Here, we report depth-resolved chemical speciation of a W-B_4C multilayer structure using combined XRR and GIXRF measurements along with the XSW-assisted depth-resolved x-ray absorption near-edge structure (XANES) measurements. The depth selectivity of the XSW wave field inside the multilayer structure was controlled by precisely tuning the grazing incidence angle of the impinging x-ray wave field. We have carried out x-ray reflectometry measurements to investigate the anomalous behavior of the optical constants (δ, β) of W in the vicinity of the W-L_3 characteristic absorption edge. Such measurements are highly useful for obtaining quantitative information on the stoichiometric chemical nature and electronic distribution of the probed atom in the material. XSW-assisted depth-resolved XANES measurements near the W-L_3 absorption edge energy ($E_o \sim 10207$ eV) were carried out for two sets of W-B_4C multilayer structures comprising 10 and 15 bilayer repetitions, respectively. Our results show the existence of unusual electronic states for the W atoms that are present at the interface boundary as compared those present in the bulk thin film medium in the case of the W-B_4C multilayer structure. The GIXRD measurements performed on the same multilayer structure support the results of the XSW investigations. We also carried out detailed calculations for the density of states and XANES spectra for the bulk crystalline W using first-principles density functional theory. Its formal similarity with the measured XANES data strengthens our findings.

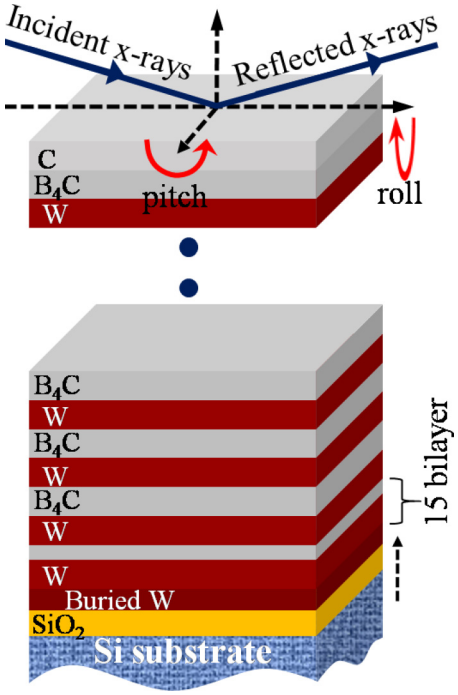

FIG. 1. A schematic representation showing the x-ray reflection from a W-B_4C multilayer structure consisting of $N = 15$ bilayer repetitions. In this figure we have also depicted a buried interface layer of W inside the multilayer medium, on top of a Si substrate.

II. EXPERIMENTAL

W-B_4C periodic multilayer structures, comprising $N = 15$ and $N = 10$ bilayers, used in the present work were prepared on a polished Si(100) substrate at room temperature using a dc magnetron sputtering system [32]. The multilayer sample was deposited using argon, as a sputtering gas medium at a constant pressure of $\sim 5 \times 10^{-3}$ mbar, whereas the base vacuum of the chamber was maintained at $\sim 2 \times 10^{-8}$ mbar before the start of the deposition process. The combined x-ray reflectivity and grazing incidence x-ray fluorescence measurements for the W-B_4C multilayer consisting of 15 bilayer repetitions were carried out at the x-ray reflectometer station of the BL-16 beamline of the Indus-2 synchrotron facility at an incident x-ray energy of 10230 eV, monochromatized using a Si(111) double crystal monochromator [33]. A schematic illustration of the x-ray reflection from a periodic multilayer structure comprising $N = 15$ bilayer repetitions is shown in Fig. 1. The XSW-assisted depth-resolved XANES measurements at W-L_3 absorption edge energy ($E_o \sim 10207$ eV) for the W-B_4C multilayer of 15 bilayer repetitions was performed at the same reflectometer station. An x-ray beam of size 100 μm (v) $\times$ 10 mm (h), generated using a crossed-slits aperture, was allowed for the GIXRF-XANES measurements. To measure specularly reflected x-rays from a sample reflector, an avalanche photodiode (APD) detector was used. The APD detector was placed $\sim$350 mm away from the sample position. The low noise and high dynamic range of the APD detector allowed us to record XRR patterns with a dynamic range of up to $\sim$7 orders. A vortex spectroscopy detector (SDD) comprising an active surface area of 50 mm^2 and having an energy resolution of $\sim$140 eV at 5.9 keV (Mn Kα x-rays) was placed in the plane of sample substrate at a distance 25 mm [34]. Fluorescence x-rays were measured through an Al pinhole collimator of diameter $\sim$1 mm to maintain a constant solid angle of the SDD detector on the sample surface [35]. The details about the BL-16 reflectometer station are described elsewhere [33,36]. We have also carried out the XSW-XANES measurements for a W-B_4C multilayer consisting of $N = 10$ bilayer repetitions at the International Atomic Energy Agency (IAEA) GIXRF-XRR experimental facility (IAEAXspe) operated at the XRF beamline of Elettra Sincrotrone Trieste (BL-10.1L) [37]. GIXRD measurements were carried out at the angle dispersive x-ray diffraction (ADXRD) beamline (BL-12) of the Indus-2 synchrotron facility at an incident x-ray energy of 15.5 keV [38].

III. RESULTS AND DISCUSSION

A. XRR-GIXRF characterization

Figures 2(a) and 2(b), respectively, show the measured and fitted XRR and GIXRF profiles in the vicinity of the first Bragg peak for the W-B_4C multilayer structure consisting of 15 bilayer repetitions at 10230 eV incident x-ray energy (above the W-L_3 absorption edge energy $E_o \sim 10207$ eV). Simultaneous fitting of the measured XRR and GIXRF data were carried out using the CATGIXRF program [39]. During the model fitting of the experimental XRR and GIXRF profiles we have considered a thin buried layer of W of thickness 16.6 Å, inside the multilayer structure. A schematic illustration showing the location of the W buried layer is given in Fig. 1. The microstructural parameters of the W-B_4C multilayer structures comprising a number of bilayer

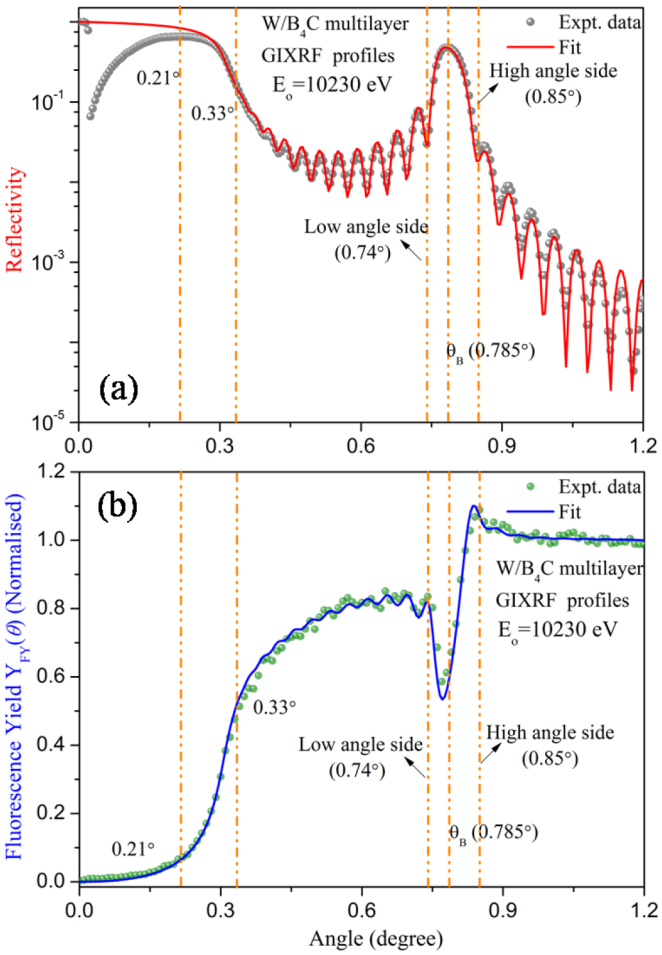

FIG. 2. Measured and fitted XRR and W-Lα fluorescence profiles for the W-B_4C multilayer structure comprising $N = 15$ bilayer repetitions at an incident x-ray energy of 10230 eV. (a) XRR profile and (b) W-Lα fluorescence profile.

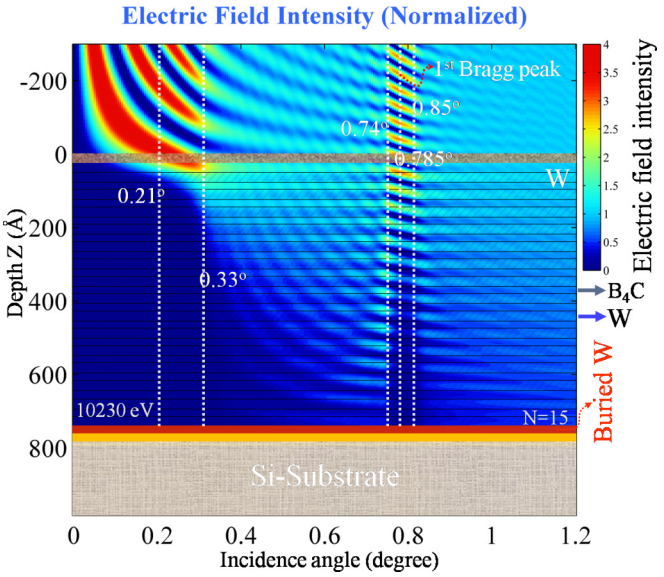

FIG. 3. X-ray field intensity (EFI) distribution inside a W-B_4C periodic multilayer structure computed using best-fitted parameters obtained from the XRR and W-Lα fluorescence measurements at an incident x-ray energy of $E = 10230$ eV. In this figure, we have also marked various dotted vertical lines showing different incident angles that have been chosen for depth selective XANES measurements of the W-B_4C multilayer structure.

repetitions $N = 15$ and $N = 10$ were determined using the combined XRR-GIXRF measurements. The best fit results give an average multilayer bilayer period thickness of $d = d_W + d_{B_4C} = 47.7$ Å with individual thicknesses of W and B_4C layers of $d_W \sim 25.4$ Å and $d_{B_4C} \sim 22.3$ Å, respectively. Detailed analysis of these multilayer structures is presented elsewhere [13]. Figure 3 depicts the computed electric field intensity (EFI) distribution at 10230 eV x-ray energy inside the W-B_4C periodic multilayer structure as a function of incidence angle and film depth (z). The EFI was computed taking into account the microstructural parameters determined from the best-fit results obtained using combined XRR and GIXRF analysis. From Fig. 3, it can be observed that the positions of XSW antinodes vary inside the multilayer medium as grazing incidence angles of the primary x-ray beam are changed. The observed periodic Kiessig interference fringes in the XRR and GIXRF profiles are anticorrelated in nature. It can be seen from Fig. 2(b) that the W-Lα fluorescence intensity profile shows a strong XSW modulation especially at the low and high angle sides of the Bragg region. The W-Lα fluorescence intensity is minimum at very low grazing incidence angles and starts increasing rapidly as the grazing incidence angle just crosses the critical angle ($\theta_c \approx 0.29°$) of the film medium. This variation of the W-Lα fluorescence intensity mainly arises due to the movement of the XSW wave field in the thin film structure. At very low grazing incidence angles or below the critical angle ($\theta_c \approx 0.29°$), there is no appreciable x-ray intensity inside the multilayer medium, but it exists only on top of the multilayer surface in the form of XSW fringes due to strong reflection (total external reflection region) from the sample surface. So, a very few W atoms, situated 2–5 nm below the top surface of multilayer, are excited by the evanescent wave and the corresponding fluorescence intensity is very weak. As the incidence angle advances through the critical angle boundary, the x-ray field starts to penetrate different layers of the multilayer medium and consequently the W-Lα fluorescence intensity increases very rapidly. At the Bragg angle ($\theta_{\text{Bragg}} \approx 0.785°$), an XSW field of periodicity equal to the multilayer period ($\Delta = d$) is set up inside the multilayer medium. At the low angle side ($\theta_{\text{Low}} \approx 0.74°$) of the Bragg peak, the antinodes of the XSW field remain in the low Z layer (B_4C layer). As the incidence angle advances across the Bragg region, these antinodes move towards the high Z layer (W layer). However, at the Bragg peak the antinodes stand exactly at the interface of the low Z and high Z layers. At the high angle side ($\theta_{\text{High}} \approx 0.85°$) of the Bragg peak, XSW antinodes completely coincide with the position of the high Z layers (W layer). Because of this movement of the XSW antinodes intensity, the W-Lα fluorescence intensity is strongly modulated over the Bragg region. As a result, at the high angle side of the Bragg peak, we obtained a relatively higher W-Lα fluorescence yield as compared to that of the low angle side. At higher incidence angles (after the first Bragg peak) the W-Lα fluorescence yield more or less remains constant because the W atom is excited only with

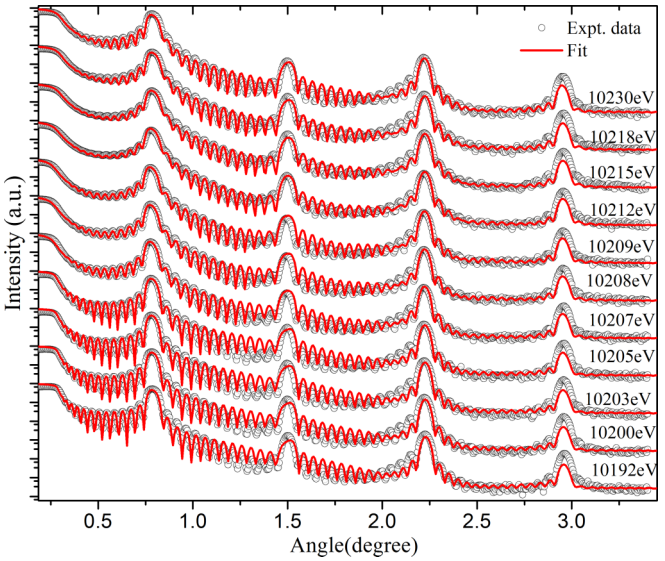

FIG. 4. Measured and fitted XRR profiles for a W-B_4C multilayer structure comprising $N = 15$ bilayer repetitions at incident x-ray energies of 10192–10230 eV.

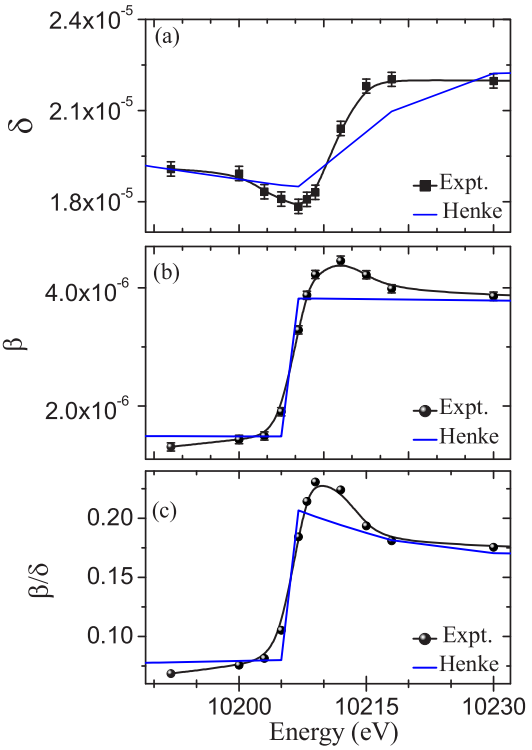

FIG. 5. Determined optical constants (a) δ and (b) β, and (c) the ratio β/δ of W from the x-ray reflectivity measurements in a W-B_4C multilayer structure comprising $N = 15$ bilayer repetitions in an x-ray energy region of 10192–10230 eV. The values of optical constants calculated from the Henke table are also given for comparison.

the direct x-ray beam as there is no formation of XSW field due to a very weak reflected x-ray beam at high incidence angles. One may expect a light XSW modulation of the W-Lα fluorescence yield near the second Bragg peak. This control depth selectivity of the XSW field in combination with x-ray absorption fine-structure analysis provides a possibility to determine the depth-selective chemical speciation of a thin film medium. This can be achieved by measuring the XSW-assisted fluorescence intensity from a thin-layered medium across the characteristic absorption edge of a layered material. We have selected various grazing incidence angles for the XSW-assisted depth-resolved x-ray absorption measurements near the W-L_3 absorption edge energy ($E_o \sim 10207$ eV). These angles are marked by the dotted vertical lines in Figs. 2 and 3. It may be important to mention here that the probed depth volume estimation from the XSW field is usually not constant across the absorption edge of a material due to the anomalous behavior of the complex refractive indices or optical constants of the layered material.

B. XRR determination of W optical constants

In order to investigate the anomalous behavior of the optical constants (δ,β) of W near the characteristic L_3 absorption region, we have performed x-ray reflectivity measurements of the W-B_4C multilayer structure near the W-L_3 absorption energy region. Figure 4 shows the measured and fitted specular reflectivity profiles of the W-B_4C multilayer structure in the energy region of 10192 to 10230 eV. The x-ray reflectivity data were recorded with an angular step size of $\theta \approx 0.005^\circ$ using the reflectometer station of the BL-16 beamline of the Indus-2 synchrotron facility. Before XRR measurements, incident x-ray energies emitted from the BL-16 beamline were calibrated by performing absorption edge measurements of a pure W foil as well as a W thin film of thickness 270 Å. While fitting XRR profiles in the energy region of 10192–10230 eV, as an initial guess we have considered the measured optical constants (δ,β) of a pure W thin film. In addition, we fixed the microstructural parameters of the W-B_4C multilayer structure and allowed the optical constants of W to vary in a controlled manner until we obtained best-fit curves to the measured XRR data. It can be seen from Fig. 4 that the measured XRR patterns match quite well with the fitted profiles except for a subtle difference at the second and fourth Bragg peak locations. This deviation can be attributed to the nonlinear diffused scattering background produced from the multilayer sample. In addition, we also recognized that the 15th bilayer period of the W-B_4C multilayer structure ($N = 15$) is slightly asymmetric, since an additional buried layer of W was created unintentionally during the deposition process. This nonuniformity in the bilayer period thickness results in a subtle difference between the measured and fitted XRF profiles at the second and fourth Bragg peaks. A detailed discussion is presented elsewhere [13]. The reflectivity of the first Bragg peak decreases significantly near the L_3 absorption edge region of W due to strong anomalous absorption effects.

The average optical constants of W in the energy region of 10192–10230 eV have been determined experimentally by fitting the measured angle-dependent specular x-ray reflectivity profiles of the W-B_4C multilayer structure. Measured values of the optical constants (δ,β) of W are plotted in Figs. 5(a) and 5(b), respectively. For comparison, we have also plotted Henke tabulated values of optical constants of W in Fig. 5 considering a density of W ~ 17.3 g/cm^3. It can be seen from Fig. 5 that the measured optical constants (δ,β) in the energy

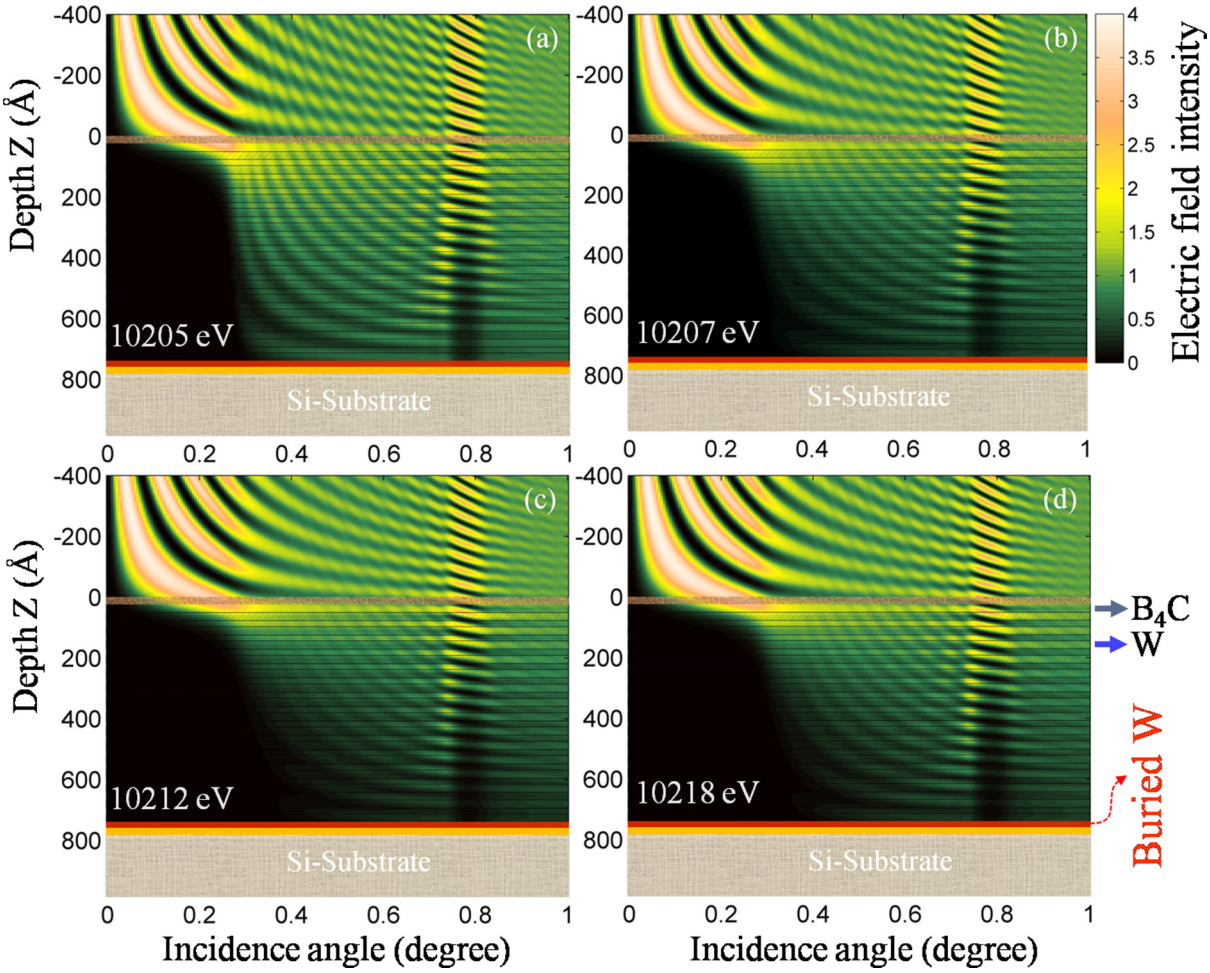

FIG. 6. X-ray field intensity (EFI) distribution inside a W-B_4C periodic multilayer structure computed using best-fitted parameters obtained from the XRR and W-Lα fluorescence measurements and determined optical constants (δ,β) at incident x-ray energies of (a)10205 eV, (b) 10207 eV, (c) 10212 eV, and (d) 10218 eV. One can clearly observe that the proving depth volume of the XSW wave field inside the W-B_4C multilayer structure across the W-L_3 absorption edge energy preserves a more or less constant volume, except for an angular shift of $\theta \sim 0.01^\circ$ at the high energy side ($E \sim 10230$ eV) of the W-L_3 edge.

region of 10192 to 10230 eV show a good agreement with the Henke tabulated values. We have observed a maximum deviation of ~5%–7% between measured and tabulated values of δ, whereas in the case of β values a maximum deviation of ~10%–15% was realized. In the case of x-ray reflectivity analysis, the measurement accuracies of the optical constants usually depend on the β/δ ratio for all the materials [40,41]. The optical constants can be uniquely determined in a situation when $\beta/\delta \leqslant 0.5$. Figure 5(c) shows the variation of the β/δ ratio of W in our case for the energy region of 10192 to 10230 eV. At a first glance, this variation seems to be in close agreement with the Henke tabulated values. We observe a maximum variation in the β/δ ratio of W ~0.23. In order to investigate the dependency of the probed depth volume of the XSW field at different incident x-ray energies and grazing incidence angles, we have computed the EFI distribution in the vicinity of the L_3 absorption edge of W. Figure 6 represents the computed EFI distribution at (a) 10205 eV, (b) 10207 eV, (a) 10212 eV, and (a) 10218 eV x-ray energies inside the W-B_4C multilayer structure as a function of incidence angle and film depth (z). The EFI was computed taking into account the fitted microstructural parameters of the multilayer structure and derived optical constants obtained from the XRR analysis at different x-ray energies. From Fig. 6, it can be observed that the probed depth of the x-ray field inside the multilayer structure remains more or less constant in the case where incident x-ray energies are varying in the vicinity of the W-L_3 absorption edge. However, the location of XSW antinodes shift by an angle of 0.01° for x-ray energies above the L_3 absorption edge ($E \sim 10218$ eV).

C. XSW-assisted XANES for depth-resolved analysis

Figures 7(a) and 7(b), respectively, show the measured and normalized XSW-assisted depth-resolved x-ray absorption near edge structure measurements for two different W-B_4C multilayer structures consisting of 15 and 10 bilayer repetitions at various grazing incidence angles in the vicinity of the L_3 edge energy of tungsten. In this figure, we have also plotted the measured XANES profile (in the fluorescence mode) of a pure tungsten metal foil. The main absorption peak (white line) in Figs. 7(a) and 7(b) is visible due to strong transition of

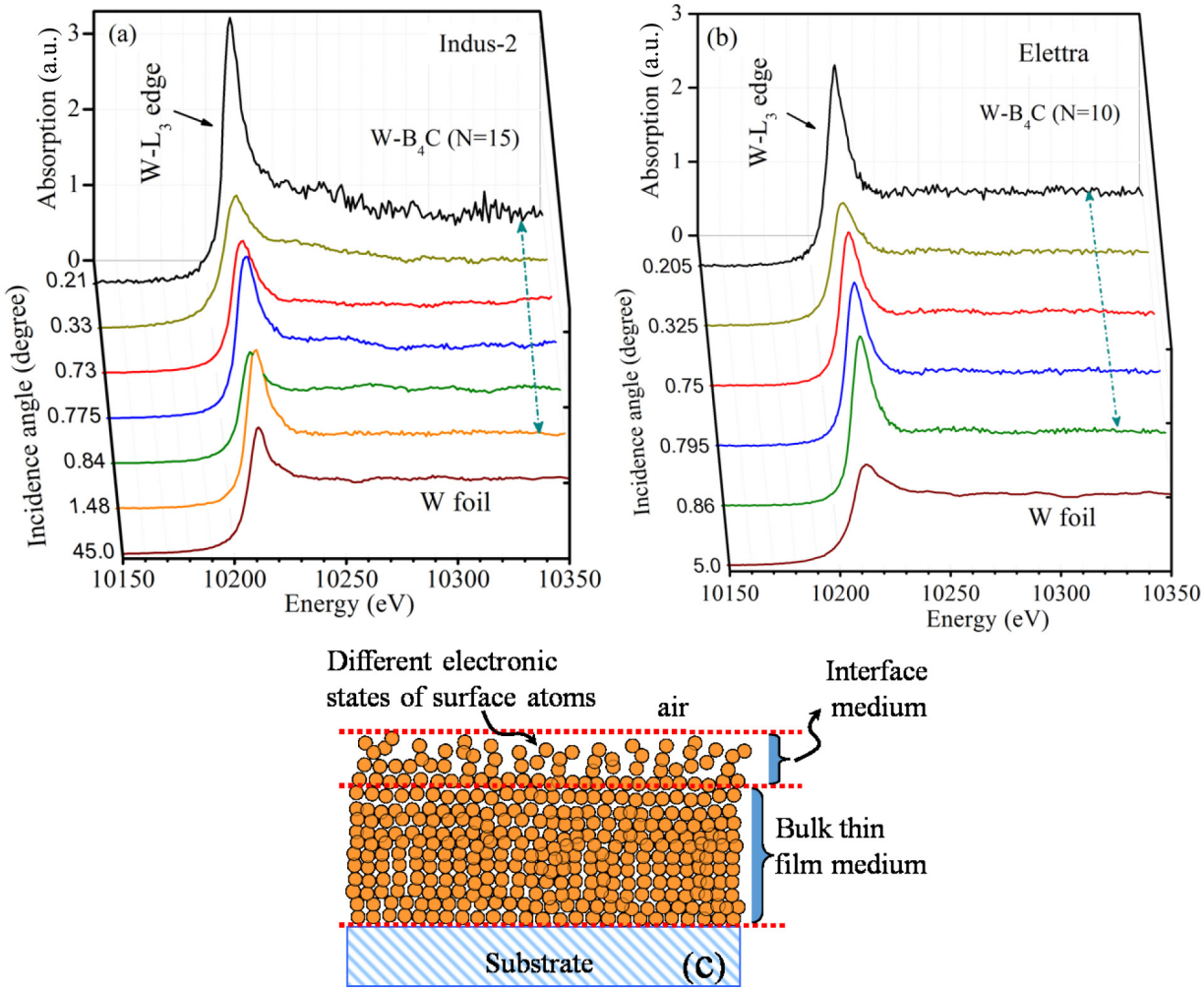

FIG. 7. X-ray standing-wave-induced XANES profiles of the W-B_4C multilayer structures measured at the L_3 edge of W. (a) Measured XANES profile of a multilayer structure consisting of $N = 15$ bilayer repetitions using the BL-16 beamline of the Indus-2 synchrotron facility. (b) W-B_4C B multilayer structure with $N = 10$ bilayer repetitions measured at the IAEA GIXRF-XRR experimental facility (IAEAXspe) operated at the XRF beamline of Elettra Sincrotrone Trieste (BL-10.1L). On the right-hand side, (c) a schematic illustration depicts the real space distribution of W atoms at the surface-interface boundary as well as inside the bulk thin film medium.

$2p_{3/2}$ electrons to the partially filled $5d$ levels [see Fig. 9(a)]. It can also be seen here that the peak intensity of the white line varies at various grazing incidence angles. This is mainly attributed to different probing depths (i.e., extinction lengths) of the x-ray wave field inside the W-B_4C multilayer structure at different grazing incidence angles. The observed white line features in measured XANES profiles of the W-B_4C multilayer structure ($N = 15$) at different grazing incidence angles, e.g., $\theta = 0.73^\circ$ (at the low angle side), $\theta = 0.775^\circ$ (at the first Bragg peak), and $\theta = 0.84^\circ$ (at the high angle side), correspond to different probing depths of the x-ray wave field. At these incidence angles, antinodes of the XSW field exist in the low Z layers (B_4C), at the interface of the B_4C-W layers, and in the high Z layers (W), respectively. The white line intensity at the incidence angle of $\theta = 1.48^\circ$ (at the second Bragg peak) describes a normal excitation of the W-B_4C multilayer structure. This is due to the fact that at such a high incidence angle the XSW field does not exist inside the multilayer structure because of the very weak reflection of the primary x-ray beam. In this condition, all the W layers of the multilayer are excited only by the primary x-ray beam. It can also be seen that the characteristic feature of the white line at $\theta = 1.48^\circ$ is similar to that of the pure W metal foil. On the other hand, a subtle shift of the edge energy position ($E_o = 10207$ eV) can be observed in the measured XANES profiles at grazing incidence angles of 0.21° and 0.33°. This occurs mainly due to the small probing depth of the XSW wave field inside the multilayer medium at these angles. Under such conditions only a few W atoms sitting at the top surface of a tungsten layer are excited. These top subsurface W atoms experience a highly asymmetric crystal environment, which in turn decreases their binding energy as compared to those of W atoms, situated at deep inside the multilayer medium. It can also be noticed from Fig. 7 that, at lower grazing incidence angles, the peak intensity of the white line is relatively larger as compared to that of the higher incidence angles. This can be explained by understanding the origin of the white line that arises as a result of the electron transition from W-$2p_{3/2}$ orbitals to partially filled $5d$ orbitals in addition to the transitions that occur from W-$2p_{3/2}$ to unoccupied localized states near $5d$ states. These

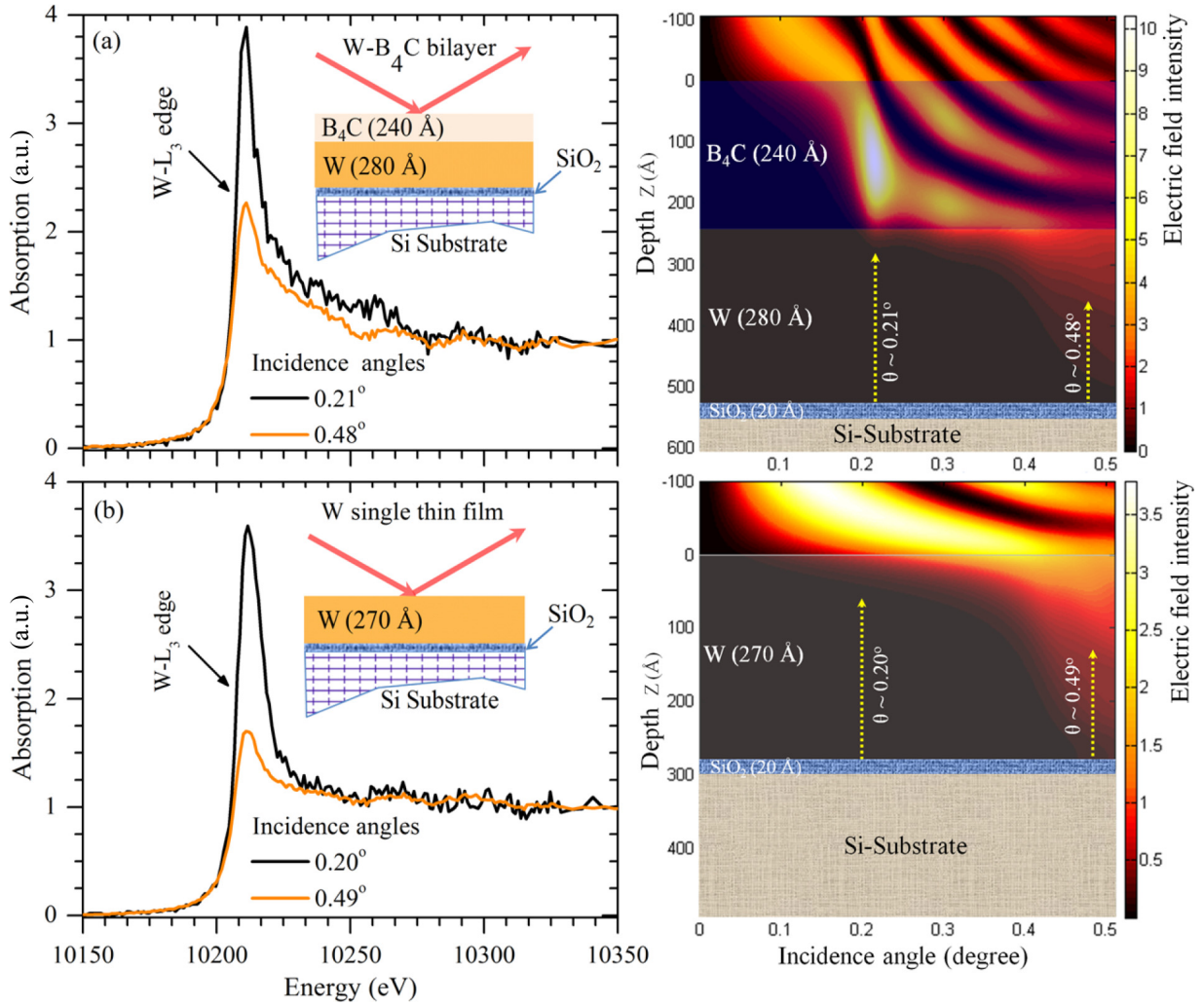

FIG. 8. X-ray standing-wave-induced XANES profiles of (a) a W-B_4C bilayer structure and (b) a W single thin film structure at the L_3 edge of W. In the insets of panels (a) and (b) schematic model structures of a W-B_4C bilayer structure and a W single thin film structure are given. On the right hand side, computed x-ray field distribution near W-L_3 edge energy ($E \sim 10208$ eV) is shown inside the two mediums.

localized states emerge because of the bulk defects as well as due to surface effects [see Fig. 7(c)]. In the case of bulk, an atom remains in a homogeneous structured environment. This causes an overlap of electron wave functions of adjacent neighboring atoms in all three directions uniformly. As a result, the dipolar coupling between the two orbitals that lead to the origin of the white line intensity is distributed nearly isotropically, whereas in the case of surface or interface states the atomic densities may be localized to their position because of lack of bulk symmetries. This would lead to sharp dipolar transitions between core levels and unoccupied surface states. The contribution of the surface effects are usually very large in the case of a thin film structure of thickness ranging in the few tens of angstroms. At the grazing incidence angle, the relative contribution of surface states will be larger as compared to that of the bulk defects, which in turn enhance the peak intensity of the white line in the normalized XANES spectra. Figure 7(b) shows the normalized XANES spectra measured at the IAEA GIXRF-XRR experimental facility operated at the XRF beamline of Elettra Sincrotrone Trieste (BL-10.1L) for a W-B_4C multilayer consisting of a number of bilayer periods, $N = 10$. We arrive at a similar conclusion after analyzing the XSW-XANES profiles presented in Fig. 7(b).

In order to further validate our conclusions drawn from the XANES analysis of the multilayer structures, we have carried out XSW-assisted XANES measurements on a W single thin film structure (thickness $d \sim 270$ Å), as well as on a W-B_4C bilayer structure (bilayer thickness $d = d_W + d_{B_4C} = 280 + 240$ Å), to determine the formation of various chemical phases (if any) inside the thin film medium. Figure 8 shows the measured XANES profiles for (a) W-B_4C bilayer and (b) W single thin film structures at various grazing incidence angles. It can be noticed from Fig. 8 that the XANES profiles of W-B_4C bilayer and W single thin film structures resemble the formal XANES nature of multilayer structures at various grazing incidence angles. On the right-hand side of Fig. 8, we have depicted the XSW field distribution inside the bilayer and single thin film structures. In these figures the probed depths of x-rays at various grazing incidence angles are marked by arrows. It confirms that the enhanced white line intensity at very low grazing incidence angles arises mainly due to the surface states and that the self-absorption effect does not

play any significant role in this particular scenario [42,43]. In conventional XANES measurements it has already been shown that the peak intensity of the white line remains more or less unchanged in the case of different oxidation states of W [27,28,44]. These XANES profiles do not provide any signature of change of the chemical state of W in the W-B_4C multilayer structures. Our results are found to be consistent with the investigations reported by Rao *et al.* [45]. They have shown that W and B_4C in the W-B_4C multilayer remain stable up to an annealing temperature of 800 °C. Beyond this temperature (above ∼1000 °C), the B_4C layer starts to decompose into free C or B atoms, which then react with the W atoms to produce more stable chemical phases of the tungsten [46].

D. *ab initio* XANES calculations and GIXRD measurements

In order to further confirm our findings we carried out first-principles studies on pure bulk crystalline bcc W (lattice parameter, 3.16 Å; space group, Im-3m). We used a plain-wave-basis-set-based density function theory (using the CASTEP module of Material studio 16.0 [47]), with an energy cutoff of 400 eV, on the fly-generated norm-conserving pseudopotential. The Brillouin zone is sampled in the k-space within the Monkhorst-Pack scheme and grid size for the SCF calculation was chosen as 16 × 16 × 16 with an SCF tolerance of 10^{-7} eV/atom. Electronic exchange correlation was treated within the generalized gradient approximation using the Perdew-Burke-Ernzerhof (PBE) functional [48]. Since it is well known that the XANES spectra maps the unoccupied density of states of a material, we display in Fig. 9(a) the atom-projected partial density of states of the W (5d). The form of the density of states as a function of energy would predict an overall nature of the XANES spectra and their formal similarity is clearly visible in Fig. 9(b). In Fig. 9(b) we present the simulated L_3 absorption spectra of pure bulk crystalline bcc W for two different core-level broadenings (τ), 10.0 eV (black solid line) and 15.0 eV (red solid line), respectively. The clear resemblance between the theoretically calculated XANES of pure bulk W crystal and that of the experimentally observed spectrum presented in Fig. 7 confirms our hypothesis and clearly shows no significant signature changes in the chemical state of W. The theoretical spectrum with $\tau = 15.0$ eV (red solid line) matches nicely with that of the experimental results. This suggests a larger core level broadening of W.

We have also carried out GIXRD measurements for the W-B_4C multilayer at 15.5 keV x-ray energy to determine the formation of various crystalline phases (if any) inside the multilayer medium. Figure 10 shows the measured GIXRD pattern of the W-B_4C multilayer consisting of $N = 15$ bilayer repetitions at a fixed grazing incidence angle of 1°. It may be noted here that the attenuation length of the incident x-ray at 15.5 keV is greater than the total thickness of the W-B_4C multilayer stack. The GIXRD measurements show two broad peaks corresponding to the W(110) and W(211) planes, which suggest that W is present in the polycrystalline phase with a very small grain size boundary. We can also observe a very small peak at ∼29.9° that arises due to asymmetric reflection from the Si substrate. The GIXRD measurement does not provide any evidence of formation of any other chemical phases of the W inside the W-B_4C multilayer structure.

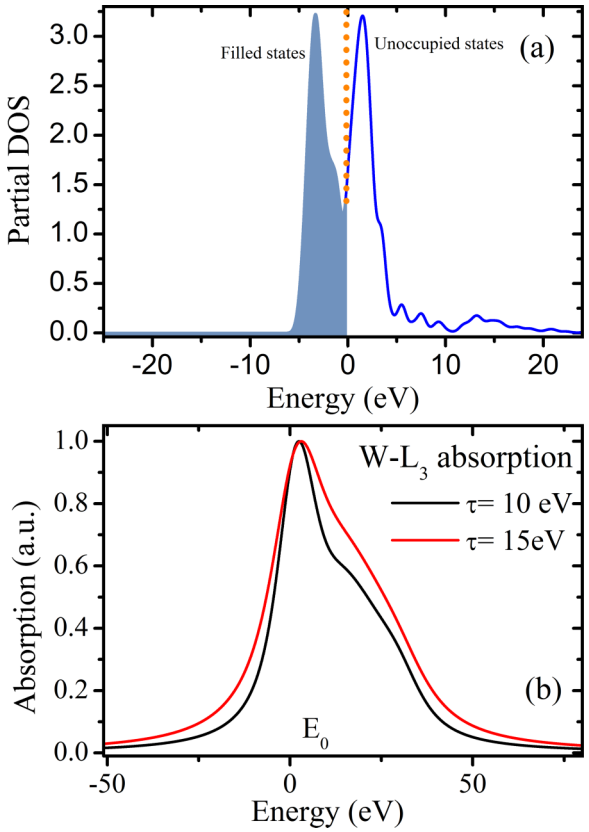

FIG. 9. First-principles simulated (a) partial density of states of W (5d) and (b) core level (L_3) absorption spectra of pure bulk bcc W.

In practice, it is very difficult to map depth-resolved chemical information on thin-layered materials by using

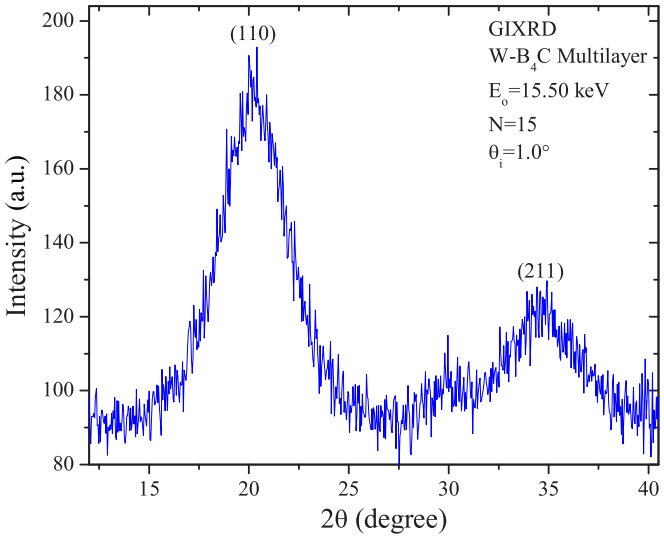

FIG. 10. Measured GIXRD pattern of a W-B_4C multilayer consisting of $N = 15$ bilayer repetitions at an incident x-ray energy of 15.5 keV. During the measurements the incidence angle of the primary x-ray beam was fixed at 1.0°.

conventional x-ray absorption fine-structure (XAFS) measurements (transmission or fluorescence mode). The combined XSW-XAFS analysis approach offers an opportunity to study the depth-resolved local structure of thin-layered materials with atomic scale resolution.

IV. CONCLUSIONS

We have demonstrated that the XANES characterization along with the combined XRR-GIXRF analysis can be used as a sensitive probe to perform depth-resolved chemical speciation of a thin film structure. We have applied this approach to investigate detailed microstructural properties of W-B_4C multilayer structures. Two sets of W-B_4C multilayer structures consisting of $N = 15$ and $N = 10$ bilayer periods have been analyzed using the Indus-2 synchrotron and Elettra Sincrotrone Trieste facilities. XSW-XANES results reveal significant changes in the chemical nature of W atoms that are present at the surface and interfaces as compared with those present in the bulk thin film medium. This is mainly due to the surface electronic states of the W atoms. On the other hand, the electronic behavior of the W atoms that are present deep inside the bulk W layer remains unchanged, which represents the bulk electronic states of W. This is further confirmed through the first-principles calculations carried out on bulk crystals of W. The grazing incidence x-ray diffraction results also support the abovementioned conclusions. The understanding of distribution of surface states as a function of depth for thin films is often necessary to correlate electronic, magnetic and transport properties of a thin film device.

ACKNOWLEDGMENTS

The authors acknowledge Sh. M. N. Singh, Synchrotrons Utilization Section, for his help with the GIXRD measurements. The authors thank Professor S. Pascarelli, European Synchrotron Radiation Facility, Grenoble-France, for fruitful discussions and suggestions. The authors are deeply indebted to Elettra Sincrotrone Trieste for successful beam time under the International Atomic Energy Agency (IAEA) beam time quota. One of the authors, G.D., would like to thank the Homi Bhabha National Institute, India, for providing support through a research fellowship.

[1] J. Chakhalian, J. W. Freeland, H. U. Habermeier, G. Cristiani, G. Khaliullin, M. van Veenendaa, and B. Keimer, Science **318**, 1114 (2007).

[2] N. Nakagawa, H. Y. Hwang, and D. A. Muller, Nat. Mater. **5**, 204 (2006).

[3] E. Benckiser *et al.*, Nat. Mater. **10**, 189 (2011).

[4] A. D. Rata, A. Herklotz, K. Nenkov, L. Schultz, and K. Dorr, Phys. Rev. Lett. **100**, 076401 (2008).

[5] G. Jackeli and G. Khaliullin, Phys. Rev. Lett. **101**, 216804 (2008).

[6] A. Tebano, C. Aruta, S. Sanna, P. G. Medaglia, G. Balestrino, A. A. Sidorenko, R. De Renzi, G. Ghiringhelli, L. Braicovich, V. Bisogni, and N. B. Brookes, Phys. Rev. Lett. **100**, 137401 (2008).

[7] C. Aruta, G. Ghiringhelli, V. Bisogni, L. Braicovich, N. B. Brookes, A. Tebano, and G. Balestrino, Phys. Rev. B **80**, 014431 (2009).

[8] M. Salluzzo, J. C. Cezar, N. B. Brookes, V. Bisogni, G. M. De Luca, C. Richter, S. Thiel, J. Mannhart, M. Huijben, A. Brinkman, G. Rijnders, and G. Ghiringhelli, Phys. Rev. Lett. **102**, 166804 (2009).

[9] S. Bera, K. Bhattacharjee, G. Kuri, and B. N. Dev, Phys. Rev. Lett. **98**, 196103 (2007); P. Yu, J. S. Lee, S. Okamoto, M. D. Rossell, M. Huijben, C. H. Yang, Q. He, J. X. Zhang, S. Y. Yang, M. J. Lee, Q. M. Ramasse, R. Erni, Y. H. Chu, D. A. Arena, C. C. Kao, L. W. Martin, and R. Ramesh, *ibid.* **105**, 027201 (2010).

[10] M. Zwiebler, J. E. Hamann-Borrero, M. Vafaee, P. Komissinskiy, S. Macke, R. Sutarto, F. He, B. Büchner, G. A. Sawatzky, L. Alff, and J. Geck, New J. Phys. **17**, 083046 (2015); A. L. Dadlani, S. Acharya, O. Trejo, F. B. Prinz, and J. Torgersen, ACS Appl. Mater. Interfaces **8**, 14323 (2016).

[11] J. Mannhart and D. G. Schlom, Science **327**, 1607 (2010); B. Revaz, M. C. Cyrille, B. L. Zink, I. K. Schuller, and F. Hellman, Phys. Rev. B **65**, 094417 (2002).

[12] T. Okumura, T. Nakatsutsumi, T. Ina, Y. Orikasa, H. Arai, T. Fukutsuka, Y. Iriyama, T. Uruga, H. Tanida, Y. Uchimoto, and Z. Ogumi, J. Mater. Chem. **21**, 10051 (2011); C. Jia, Q. Liu, C. Sun, F. Yang, Y. Ren, S. M. Heald, Y. Liu, Z. Li, W. Lu, and J. Xie, ACS Appl. Mater. Interfaces **6**, 17920 (2014).

[13] G. Das, A. Khooha, A. K. Singh, A. K. Srivastava, and M. K. Tiwari, Appl. Phys. Lett. **108**, 263109 (2016).

[14] J. R. Church, C. Weiland, and R. L. Opila, Appl. Phys. Lett. **106**, 171601 (2015).

[15] J. B. Kortright and A. Fischer-Colbrie, J. Appl. Phys. **61**, 1130 (1987); Y. Wang, S. Narayanan, J. Liu, D. Shu, A. Mashayekhi, J. Qian, and J. Wang, J. Synchrotron Radiat. **14**, 138 (2007).

[16] H. Wang, S. S. Dhesi, F. Maccherozzi, S. Cavill, E. Shepherd, F. Yuan, R. Deshmukh, S. Scott, G. van der Laan, and K. J. S. Sawhney, Rev. Sci. Instrum. **82**, 123301 (2011); M. A. MacDonald, F. Schaefers, R. Pohl, I. B. Poole, A. Gaupp, and F. M. Quinn, *ibid.* **79**, 025108 (2008).

[17] P. C. Pradhan, D. Gangir, A. Majhi, M. Nayak, A. Biswas, D. Bhattacharyya, and G. S. Lodha, J. Phys. D: Appl. Phys. **49**, 135305 (2016); D. L. Windt, E. M. Gullikson, and C. C. Walton, Opt. Lett. **27**, 2212 (2002).

[18] A. Joshua, S. Pecker, J. Ruhman, E. Altman, and S. Ilani, Nat. Commun. **3**, 1129 (2012).

[19] M. K. Tiwari, K. J. S. Sawhney, T.-L. Lee, S. G. Alcock, and G. S. Lodha, Phys. Rev. B **80**, 035434 (2009); M. K. Tiwari, H. Wang, K. J. S. Sawhney, M. Nayak, and G. S. Lodha, *ibid.* **87**, 235401 (2013); J. D. Emery, B. Detlefs, H. J. Karmel, L. O. Nyakiti, D. K. Gaskill, M. C. Hersam, J. Zegenhagen, and M. J. Bedzyk, Phys. Rev. Lett. **111**, 215501 (2013); J. A. Libera, H. Cheng, M. O. de la Cruz, and M. J. Bedzyk, J. Phys. Chem. B **109**, 23001 (2005).

[20] J. Zegenhagen and A. Kazimirov, *The X-Ray Standing Wave Technique: Principle and Applications* (World Scientific, Singapore, 2013).

[21] Y. Kayser, J. Sa, and J. Szlachetko, Anal. Chem. **87**, 10815 (2015).
[22] D. C. Meyer, K. Richter, P. Paufler, P. Gawlitza, and T. Holz, J. Appl. Phys. **87**, 7218 (2000).
[23] D. C. Meyer, P. Gawlitza, K. Richter, and P. Paufler, J. Phys. D: Appl. Phys. **32**, 3135 (1999).
[24] B. Pollakowski, B. Beckhoff, F. Reinhardt, S. Braun, and P. Gawlitza, Phys. Rev. B **77**, 235408 (2008).
[25] B. Pollakowski, P. Hoffmann, M. Kosinova, O. Baake, V. Trunova, R. Unterumsberger, W. Ensinger, and B. Beckhoff, Anal. Chem. **85**, 193 (2013).
[26] K. Sanyal, A. Khooha, G. Das, M. K. Tiwari, and N. L. Misra, Anal. Chem. **89**, 871 (2017).
[27] E. Oakton, G. Siddiqi, A. Fedorov, and C. Coperet, New J. Chem. **40**, 217 (2016).
[28] U. Jayarathne, P. Chandrasekaran, A. F. Greene, J. T. Mague, S. DeBeer, K. M. Lancaster, S. Sproules, and J. P. Donahue, Inorg. Chem. **53**, 8230 (2014).
[29] F. J. Garcia-Garcia, J. Gil-Rostra, F. Yubero, J. P. Espinós, and A. R. Gonzalez-Elipe, J. Phys. Chem. C **119**, 644 (2015).
[30] V. Luca, M. G. Blackford, K. S. Finnie, P. J. Evans, M. James, M. J. Lindsay, M. Skyllas-Kazacos, and P. R. F. Barnes, J. Phys. Chem. C **111**, 18479 (2007); D. E. Clinton, D. A. Tryk, I. T. Bae, F. L. Urbach, M. R. Antonio, and D. A. Scherson, J. Phys. Chem. **100**, 18511 (1996); S. Yamazoe, Y. Hitomi, T. Shishido, and T. Tanaka, J. Phys. Chem. C **112**, 6869 (2008).
[31] S. A. Ganus, X-ray spectroscopic study of tungsten compounds, Ph.D. thesis, Department of Physics, Goa University, India, 1996.
[32] M. Nayak, P. N. Rao, and G. S. Lodha, Asian J. Phys. **19**, 1 (2010).
[33] G. Das, S. R. Kane, A. Khooha, A. K. Singh, and M. K. Tiwari, Rev. Sci. Instrum. **86**, 055102 (2015); G. Das, A. Khooha, S. R. Kane, A. K. Singh, and M. K. Tiwari, AIP Conf. Proc. **1728**, 020142 (2016).
[34] G. Das, M. K. Tiwari, A. K. Singh, and H. Ghosh, J. Anal. At. Spectrom. **29**, 2405 (2014).
[35] W. Li, J. Zhu, X. Ma, H. Li, H. Wang, K. J. S. Sawhney, and Z. Wang, Rev. Sci. Instrum. **83**, 053114 (2012).
[36] M. K. Tiwari, P. Gupta, A. K. Sinha, S. R. Kane, A. K. Singh, S. R. Garg, C. K. Garg, G. S. Lodha, and S. K. Deb, J. Synchrotron Radiat. **20**, 386 (2013).
[37] P. M. Wrobel, M. Bogovac, H. Sghaier, J. J. Leani, A. Migliori, R. Padilla-Alvarez, M. Czyzycki, J. Osan, R. B. Kaiser, and A. G. Karydas, Nucl. Instr. and Meth. in Phys. Res. A **833**, 105 (2016).
[38] A. K. Sinha, A. Sagdeo, P. Gupta, A. Upadhyay, A. Kumar, M. N. Singh, R. K. Gupta, S. R. Kane, A. Verma, and S. K. Deb, J. Phys.: Conf. Ser. **425**, 072017 (2013).
[39] M. K. Tiwari and G. Das, X-Ray Spectrom. **45**, 212 (2016).
[40] J. M. Andre, R. Barchewitz, A. Maquet, and R. Marmoret, Phys. Rev. B **29**, 6576 (1984).
[41] R. Soufli and E. M. Gullikson, Appl. Opt. **36**, 5499 (1997).
[42] P. Pfalzer, J. P. Urbach, M. Klemm, S. Horn, M. L. denBoer, A. I. Frenkel, and J. P. Kirkland, Phys. Rev. B **60**, 9335 (1999).
[43] W. Li, X. Yuan, J. Zhu, J. Zhu, and Z. Wang, Phys. Scr. **90**, 015804 (2015).
[44] P. C. Pradhan, A. Majhi, M. Nayak, M. Nand, P. Rajput, D. K. Shukla, A. Biswas, S. K. Rai, S. N. Jha, D. Bhattacharyya, D. M. Phase, and N. K. Sahoo, J. Appl. Phys. **120**, 045308 (2016).
[45] P. N. Rao, S. K. Rai, M. Nayak, and G. S. Lodha, Appl. Opt. **52**, 6126 (2013).
[46] P. Siffalovic, M. Jergel, L. Chitu, E. Majkova, I. Matko, S. Luby, A. Timmann, S. V. Roth, J. Keckes, G. A. Maier, A. Hembd, F. Hertlein, and J. Wiesmann, J. Appl. Crystallogr. **43**, 1431 (2010).
[47] S. Clerck *et al.*, Z. Kristallogr. **220**, 567 (2005).
[48] J. P. Perdew, K. Burke, and M. Ernzerhof, Phys. Rev. Lett. **77**, 3865 (1996).